A Hierarchical Model for the Computation of Permeation Properties of Porous Materials and Their Enhancement due to Microcracks

Fadi Khaddour, David Grégoire, Gilles Pijaudier-Cabot

Accepted manuscript in Journal of Engineering Mechanics. DOI: 10.1061/(ASCE)EM.1943-7889.0001392
The final publication is available at: https://dx.doi.org/10.1061/(ASCE)EM.1943-7889.0001392

A hierarchical model for the computation of enhanced permeation properties of porous materials due to micro-cracks

by

Fadi Khaddour[1], David Grégoire[2], and Gilles Pijaudier-Cabot[3], A.M. ASCE

ABSTRACT: This paper presents a model capable to provide estimates of the apparent permeability directly from the pore size distribution and from the properties of the fluid to be considered. The model is based on a hierarchical assembly of capillaries with decreasing diameter, generated randomly. The technique yields a porous network, which mimics the pore space measured experimentally by mercury intrusion. The intrinsic permeability and the evolution of the apparent permeability with mean pressure are provided by equating Darcy's law and a combination of Poiseuille's and Knudsen's laws. Comparisons with experimental data on mortar specimens show that the model provides the intrinsic permeability and its evolution when the material is subjected to mechanical loads. For a given pore size distribution, the evolution of the apparent permeability is also provided and test data with several types of gases compare quite well with the model.

[1] Laboratoire des Fluides Complexes et leurs Réservoirs, LFC-R UMR5150, Univ. Pau & Pays Adour, Allée du Parc Montaury, F64600 Anglet, France

[2] Laboratoire des Fluides Complexes et leurs Réservoirs, LFC-R UMR5150, Univ. Pau & Pays Adour, Allée du Parc Montaury, F64600 Anglet, France

[3] Laboratoire des Fluides Complexes et leurs Réservoirs, LFC-R UMR5150, Univ. Pau & Pays Adour, Allée du Parc Montaury, F64600 Anglet, France

INTRODUCTION

The relationship between the microstructure of cement, mortar and rocks and their permeation properties is a problem that has been addressed in many instances. Hydrocarbon production is a first example in which permeation properties have direct practical consequences. In most cases, the data available result from the extraction of cores during the exploration phase, and the permeability of the rock is related to its porosity. In the case of cementitious materials, what is at stake is not only the initial permeation properties of the material but also their evolution upon increasing, sustained or thermal loads. Because of micro-cracking, the permeability of the material increases (see e.g. Choinska et al. 2007). This increase is of great importance in the long-term assessment of tightness of vessels and waste containment facilities (see e.g. Jason et al. 2007).

In the literature, one may distinguish typically several approaches for estimating the permeability of a porous material.

In the first one, permeation properties are computed from pore network models. This approach allows a rather fine modelling at the pore scale in networks that are either generated randomly, e.g. on the basis of a pore size distribution using a discrete element approach (Li et al., 2016) or a lattice based model (Grassl, 2009), or taken from scanning electron microscope (SEM) images of mortar (see e.g. Wong et al. 2012, Sun et al. 2011, 2013). Finite element or discrete element calculations can be coupled with Lattice-Boltzman calculations that solve the Stoke's problem in the pore network at the subscale or extracted from digital image analysis. It allows very accurate descriptions of the flow in the pore network coupled with the applied loads (White et al. 2006).

Because the analysis is performed at the pore scale, multiphase flow and wettability considerations can be included in such models, allowing for estimates of relative permeability (see e.g. the review papers by Blunt, 2001 and Blunt et al., 2002). On the other hand, these very powerful techniques are quite computationally demanding, aside from the fact that each new state of micro-cracking in the material requires the consideration of a new pore network model.

45 The second type of approach relies on continuum based up-scaling and homogenisation theories.
46 Berndt and Sevostianov (2012) discuss several micromechanical models in which the effective
47 permeability of a heterogeneous material is derived from Darcy's law at the lower scale (Darcy,
48 1856). It results into formulas where the porosity appears in the evaluation of the effective
49 permeability of the porous material explicitly (see also Dormieux et al. 2006). Because these
50 approaches do not represent the exact distribution of pores in the material (it is rather idealised
51 through some concentration factors), they fail at capturing the effect of increasing micro-crack
52 density on permeability as connectivity and tortuosity issues may arise. Extended models have been
53 proposed for this purpose, e.g. by Chunsheng et al. (2011), based on specific micro-crack
54 configuration (parallel cracks) and Monte-Carlo simulations. A more recent approach has been
55 proposed by Timothy and Meschke (2016), in which the permeability is derived from cascade
56 micromechanics, but the choice of the cascade number that controls connectivity properties is a
57 pending issue.
58 The third type of approach is widely used in engineering applications and relies on analytical
59 formulas where the input is the characterisation of the pore size distribution. Pioneering works by
60 (Kozeny, 1927) related the permeability to the porosity, the tortuosity and an average pore size.
61 Later on, Katz and Thompson (1986) predicted the permeability from the electrical conductivity of
62 a porous material through a critical pores radius. Brown et al. (1991) provided a review of such
63 approaches that may for instance be based on probabilistic descriptions of the interconnection
64 between pores (Childs and Collis-George (1950), on percolation theory, or on combinations of both
65 (Guegen and Dienes, 1989)). More recently, several studies appeared in which the pore size
66 distribution has been modeled, e.g. with a bimodal (Aït-Mokhtar et al. 2002) or multimodal
67 distribution (Amiri et al. 2005), and then entered into some capillary bundle model. A model for the
68 calculation of the intrinsic permeability derived directly from the experimental pore size distribution
69 (PSD), without any idealization has been also proposed (Khaddour et al. 2015).

In this paper, which is an extended and upgraded version of the conference paper by Khaddour et al. (2014), we are going to follow this type of approach, mainly because our final intend is to implement such a description into very large scale computations where at each point, the permeation properties are expected to change with micro-cracking due to applied loads. Hence, our aim is to devise a fast estimation technique that will be repeated a large number of times during a single calculation. In the present contribution, we will not reach this stage and we will stay at the level of the estimation of the permeation properties as a first step towards this final objective. The essential element from which the permeation properties are going to be estimated is the PSD. The present approach should be seen as follow up of models aimed at describing the influence of damage on the pore size distribution of mortar or rocks (Arson and Pereira, 2013) in order to provide a consistent hydro-mechanical framework to the context described above. The experimental data provided may also serve validating these relationships, although providing or validating such is outside the scope of this paper.

Mercury intrusion porosimetry (MIP) is going to be used for the determination of the PSD for various states of micro-cracking. It is well known that MIP has strong biases, e.g. for the characterisation of small pores (see Diamond, 2000). Furthermore, it cannot reach occluded porosity, but in our case such a porosity does not participate to permeation. MIP should be seen here as an indicator of connectivity and permeation capacity of the pore system, and not as an accurate characterisation technique for the determination of the complete pore network of the material.

The model presented in this paper is an extension of earlier works (Khaddour et al., 2015) and relies on a hierarchical capillary bundle description of the pore network, which mimics the porous space measured experimentally with MIP. In the literature, analyses are usually restricted to the intrinsic permeability of the material and the evolution of the apparent permeability with respect to the pressure gradient and to the nature of the fluid considered are left aside (see e.g. the review paper by Hoseini et al. (2009) on the effect of stress on permeability). By apparent permeability, we mean the

value of the permeability defined in the Darcy's sense, although it is not a material property. Here, we aim at a model capable to provide estimates of the apparent permeability as a function of the (compressible) fluid mean pressure, directly from the pore size distribution and from the properties of the fluid to be considered. The intrinsic permeability and the evolution of the apparent permeability with mean pressure are provided by combining Darcy's law which represents the flow in the porous media at the macro-scale and a combination of Poiseuille's (Poiseuille, 1840) and Knudsen's laws (Steckelmacher, 1986, Ziarani and Aguilera, 2012), which capture viscous flow and pore walls – fluid interaction at the micro-scale respectively. Knudsen's effect was found to be non negligible for pores of relatively large diameters (Kast and Hohenthanner, 2000) especially for tight rocks (Rahmanian et al., 2013) and mortar. It has been shown also that for typical gases, the contributions of laminar flow and of Knudsen diffusion are of the same order for pores of diameter in the range of a few hundred of nanometers (Khaddour et al., 2015).

This paper is organized as follows: in the second section, the construction of a random assembly of capillaries from a given pore size distribution is described. Then, the basic equations and solution techniques for computing fluid flow in such capillaries are discussed. The fourth section presents experimental works in which intrinsic and apparent nitrogen permeability evolutions upon damage have been obtained on mortar specimens. At each stage of damage, the PSD of the specimen is characterised. Comparisons between these experimental results and those obtained from the hierarchical model are discussed in the last section. Additional comparisons on the prediction of permeation properties for different gases are also provided.

HIERARCHICAL CAPILLARY BUNDLE

We consider here the porous structure of mortar in a very simplified way: it consists in straight cylindrical pores of different lengths and various diameters. Assuming that the porous space has been characterized by its pore size distribution, we may relate, for each pore size, the pore length to the pore volume fraction.

121 The simple assembly consists in distributing all the pores within the material in parallel and in a
122 regular manner. The pore volume is divided into a set of capillary fibers of constant diameter and of
123 length equal to the cubic root of the total porous volume for each diameter, times the tortuosity.
124 Such an assembly is presented in Fig. 1 and permeability predictions based on such a parallel
125 assembly of pores have been discussed by (Khaddour et al., 2015) and additional fitting parameters
126 were required in order to achieve adequate results.
127 We adopt here a different approach where pores of different diameters are randomly connected to
128 each other, under the condition that in the direction of the fluid flow, a given pore may only be
129 connected to a smaller one. This hierarchical assumption is consistent with the technique
130 implemented for obtaining the PSD, based on mercury intrusion porosimetry. The aim is to devise a
131 model where the fitting parameters introduced in the simple assembly discussed by Khaddour et al.
132 (2015) are avoided. Note that the model is based upon a fully connected pore space. Hence, the
133 prediction of a percolation threshold that may be observed upon growing porosity is not possible.
134 In the present approach and in Khaddour et al. (2015) as well, the isotropy of the pore structure is
135 assumed, providing as an outcome the same permeability in all directions (or an average
136 permeability). This is a limitation embedded in the mercury intrusion technique used for obtaining
137 the PSD. Therefore, the proposed model is mainly applicable to cases where anisotropy of the pore
138 network (and of the permeability) is small. In the case of cementitious materials, the model applies
139 on samples that have not been loaded, or on samples that have been loaded, with small micro-
140 cracking, prior to the peak load in uniaxial compression typically. The comparisons that will be
141 presented in the final section of this paper shall comply with such a restriction. It should be noted
142 that serviceability analyses of nuclear reactor vessels for instance (see Jason et al. 2007) are
143 conducted under the same assumption as it is considered that through-cracks are not expected. In
144 the case of sedimentary rocks where transverse isotropy of the microstructure and of permeability
145 should be expected, It might be envisioned to assign weighting factors corresponding to the
146 directionality of the microstructure but such a possibility has not been considered in the present

paper and it is left for future considerations. For cases where extensive damage due to micro-cracking or localised cracking are observed, directionality effects on the permeability may be handled more easily by accounting on the crack aperture directly, e.g. through standard Poiseuille models (see Miehe and Mauthe, 2016, Pijaudier-Cabot et al. 2009, Chen et al. 2014).

The PSD is discretised into a finite set of pore diameters, $i = 1,2, \dots N$. Let V_t be the total porous volume, which may be organized according to the PSD into a series of volumes V_{pi} of mean diameter d_i. We may now relate, for each pore size, the total pore length L_i to the pore diameter d_i and to the pore volume fraction V_{pi} assuming that pores are cylindrical:

$$L_i = \frac{4.V_{pi}}{\pi.{d_i}^2} \quad (1)$$

This total pore length is then cut into small segments of random length ΔL_i (see Figure 2.a) comprised between 0 and the average pore length defined below. Their assembly is performed from larger pores to smaller pores. Each pore segment either creates a new assembling site, on which subsequent segment will be connected to form a single capillary, or is connected to an existing one of larger or equal diameter on an existing assembling site (Figure 2.b). We then define the average pore length L_e and a critical length L_c as

$$L_e = \sqrt[3]{V_t}\ , L_c = T.L_e \quad T = \text{tortuosity} \quad (2)$$

Throughout this study, the tortuosity will be taken equal to 1. In our description, large pores are the most important factor on permeability and therefore, the influence of the tortuosity is diminished. This assumption is also made fore the sake of simplicity. Assigning a specific tortuosity on each class of pore diameters would be possible, at the price of additional model parameters that would be very delicate to characterise. Finally, one should keep in mind that orders of magnitude are often sought for in predictions of permeability in view of its experimental and spatial variability. Thus

setting the tortuosity to 1 still provides a suitable estimate that ought to be considered as a local quantity resulting from an averaged PSD.

As soon as the sum of all pore segment lengths reaches the critical length on one capillary fiber, further segments cannot be added anymore.

The random function, which decides if the current pore segment dealt with is connected to an existing capillary (or assembling site) or creates a new one, is:

$$f(x) = \exp\left(-\frac{(x-B)}{A}\right) \text{ if } x > B, \text{ and } f(x) = 1 \text{ if } x \leq B \quad (3)$$

$f(x)$ is the probability that a new segment may create a new assembling site and subsequently a new capillary fiber. x is the index of the current pore segment dealt with i.e. the number of the pore segment comprised between 0 and the total number segments to be dealt with considering all the pore diameters, A is a parameter controlling the starting diameter when the new pore segments have almost no chance to create a new site (capillary) and B is a parameter controlling the starting diameter when the new pore segments have a chance to be connected to existing sites. If the index x is lower than B, the current pore increment is forced to create a new site ($f(x) = 1$).

When the hierarchical capillary bundle is generated, the fact that a pore segment is connected to an existing capillary (or assembling site) or creates a new one is critical in achieving a good estimate of the permeability. This reflects on the technique that is implemented in order to obtain the PSD and on the evolution of the PSD upon micro-cracking.

During mercury intrusion porosimetry, two different phases of intrusion are performed. Firstly, mercury is introduced at low pressure (from 0 MPa to 0.2 MPa). Then, mercury is introduced at high pressure (from 0.2 MPa to 200 MPa). The smaller the pores, the higher the pressure needed to introduce mercury inside the porous medium. Unfortunately, the data obtained at low pressure are very noisy and very large pores are not well characterised. These large pores drive the permeability and it can be very problematic in order to predict the permeability accurately. Usually, the solution

consists in removing the low-pressure information in the analysis. Figure 3.a presents a typical PSD obtained on the mortar used in the present study. We can see the result from the low pressure intrusion (above 5 μm) and the one from the high pressure intrusion (below 5 μm) and two peaks are observed. Upon damage, e.g. due to mechanical loads, newly created pores (open cracks) of large aperture might contribute significantly to the permeability. Therefore, there is a need to keep the low-pressure information to predict the evolution of permeability upon damage and we have implemented a specific filtering of the low-pressure information in connection with the function defined in Eq. (3). Newly created cracks are most certainly not cylindrical but they are assumed as such in our approach and in the interpretation of MIP results too. In both cases, we deal with flow into newly formed pores, whatever their shape and it is important that assumptions be the same in each case. In this way, there is no bias between the characterisation of the PSD and the permeability analysis, although the models are a rough approximation of actual pore shapes.

In order to keep the low pressure information, and therefore to account for large pores, we implement a procedure aimed at minimizing their impact on the overall permeability by making sure that capillaries of large diameter have little chance to percolate. In such a way the inaccuracies encountered during the low pressure intrusion have little effect on the overall estimation of permeability: let us consider the pores of size corresponding to the low-pressure measurements only. These pores are discretized randomly into segments of equal size. We now count the number of segment corresponding to these pore sizes. Figure 3b shows this number for several random realizations. We observe that the first 10000 segments correspond to the average number of pores segments whose diameter is large enough to be intruded during MIP at low pressure and therefore we force them to create a new assembly site instead of being connected to each other. Consequently pores of such sizes cannot percolate throughout the material and they cannot provide a dramatic overestimation of the overall permeability. Their contributions to the PSD, however, still exists in the hierarchical assembly, these 10000 segments are located at the entry of capillaries, the rest that occurs in the random generation may or may not be connected to them according to the probability

function in Eq. (3). The limit of 10000 segments depends on the specific material considered. Hence, it is set for a given material and its PSD. For the same material, and upon micro-cracking, this limit is not changed, allowing for capturing the influence of subsequent micro-cracks on the capillary generation and on the calculation of the permeability.

Accordingly, the parameter B in Eq.(3) is chosen in such a way that the first 10000 low-pressure pore segments are forced to create a new site ($f(x) = 1$). Upon damage, if meaningful information appear in the low-pressure part of the PSD, the number of increments at low-pressure will increase and then they will be taken into account automatically when $x>B$.

In the generation process, the permeability is calculated each time a capillary has reached the critical length. The contribution of this capillary to the permeability is added to the contributions of previous ones. When this contribution is less than a given percentage of the total permeability, the random process is stopped. The number of segment already assembled is N_{ass} and the rest of the pore segments are assembled into capillaries of constant diameter in order to save computer time (small pore sizes lead to a huge amount of pore segments to assemble). Their contribution is also taken into account in the global permeability.

The parameter A in Eq. (3) controls the decay of function $f(x)$. In particular, A controls the segment number above which new segments have almost no chance (say a few percent) to create a new capillary and should be connected to existing ones. Its influence on the calculation of the permeability is small if this segment number is above N_{ass} because new segments will be connected to each other anyway to form capillaries of constant diameter. The parameter A has been chosen equal to 1000 to ensure that this condition is met.

CALCULATION OF THE PERMEABILITY

The objective is now to compute the intrinsic and the apparent permeability from a given assembly of capillary fibers. The apparent permeability is obtained by equating Darcy's law, which represents the flow at the macro-scale, and Poiseuille's and Knudsen's laws, which represent the flow at the

micro-scale. This approach has already been detailed by (Khaddour et al., 2015) for a deterministic assembly of parallel pores of constant diameter. The model assumes that permeation properties are isotropic, which means that capillary bundles are randomly oriented in the porous material. As discussed in the previous section, the assumption of isotropy is a restriction of the present model. The fluid fluxes computed in this section shall be divided by three in order to compute the directional permeability and to account for isotropy, which means that the fluid flow equally in the three directions of space. Under the same assumption, we are going to extend this calculation to the case of capillaries composed of segments of decreasing diameters.

Flow in a pore of constant diameter

Let us consider a cylindrical pore of diameter d_i. The fluid flux (i.e. volume of fluid per unit time) passing through the pore of length L_e is calculated according to Poiseuille's law:

$$Q_P^v = \left(\frac{1}{2}\right)\frac{\pi}{128}\frac{d_i^4}{\mu}\frac{(P_1^2 - P_2^2)}{L_e\, P_2} \tag{4}$$

where (P_1, P_2) are the upstream and downstream pressure respectively, Q_P^v is the volume of fluid estimated at the outlet pressure and μ is the fluid dynamic viscosity. This classical expression relies on the assumption of laminar flow.

At the same time, the flow of a gas in the pore may be influenced by the pore walls. An indicator for such an interaction is the Knudsen number N_i^{Kn} defined for each pore of diameter d_i by:

$$N_i^{Kn} = \frac{\lambda}{d_i} = \left(\frac{1}{d_i}\right)\frac{R\,T}{\pi\sqrt{2}\,d_j^2\,N_{Av}\,P_m} \tag{5}$$

where $(\lambda,\ d_j, P_m)$ are the average free path, the molecule diameter and the average pressure of the considered gas respectively, and (N_{Av}) is the Avogadro's number. When the Knudsen number is

greater than one, the interaction between the walls of the pore and the gas, at the molecular level, are dominant and the fluid flow is quite different from Poiseuille's flow. The volume of fluid per unit time passing in the pore is (Steckelmacher, 1986):

$$Q_{Kn}^{v} = \frac{\pi}{12}\frac{d_i^3}{L_e}\sqrt{\left(\frac{8\,R\,T}{\pi\;M}\right)}\frac{\Delta P}{P_2} \tag{6}$$

where $\Delta P = P_1 - P_2$ is the difference between the upstream and downstream pressures. In the transition regime defined as $(0.01 < N_i^{Kn} < 1)$ the flow rate Q_{tot}^{i} through a pore (i) due to a pressure gradient ΔP is given as the sum of the viscous flow (Eq. 4) and the Knudsen's flow (Eq. 6):

$$Q_{tot}^{i} = Q_{Kn}^{i} + Q_{Kn}^{i}, \qquad Q_{tot}^{i} = \frac{\pi\, d_i^4}{L_e}\left[\frac{1}{128\,\mu} + \frac{1}{12\;d_i}\sqrt{\left(\frac{8\,R\,T}{\pi\;M}\right)}\left(\frac{1}{P_m}\right)\right]\frac{\Delta P\; P_m}{P_2} \tag{7}$$

where P_m is the average pressure $(P_1 + P_2)/2$.

Flow in a capillary with segments of decreasing diameter

In order to be applied to the present hierarchical model, the flow rate for the case of a capillary made of segments of pores with decreasing diameter needs to be calculated. A typical capillary of this type is shown in Fig. 4. Mass conservation requires that:

$$P_2\delta Q_a = \frac{\pi\, d_1^4}{L_1}\left[\frac{1}{128\,\mu} + \frac{1}{12\;d_1}\sqrt{\left(\frac{8\,R\,T}{\pi\;M}\right)}\left(\frac{1}{P_{m1}}\right)\right]\Delta P_1\; P_{m1} = \cdots =$$

$$\frac{\pi\, d_j^4}{L_j}\left[\frac{1}{128\,\mu} + \frac{1}{12\;d_j}\sqrt{\left(\frac{8\,R\,T}{\pi\;M}\right)}\left(\frac{1}{P_{mj}}\right)\right]\Delta P_j\; P_{mj} = \cdots$$

$$= \frac{\pi\, d_M^4}{L_M}\left[\frac{1}{128\,\mu} + \frac{1}{12\;d_M}\sqrt{\left(\frac{8\,R\,T}{\pi\;M}\right)}\left(\frac{1}{P_{mM}}\right)\right]\Delta P_M\; P_{mM} \tag{8}$$

where $\Delta P_j, P_{mj}$ are the difference between the upstream and downstream pressures and the average pressure in segment j respectively. Because the sum of the difference of square pressures is equal to the overall difference of the square pressures for the entire capillary, we have also:

$$\Delta P_1 \, P_{m1} + \cdots + \Delta P_j \, P_{mj+1} + \cdots + \Delta P_M \, P_{mM} = \Delta P \, P_m \tag{9}$$

Combining the two above equations, one obtains:

$$\delta Q_a = \frac{1}{\sum_{j=1}^{M} \frac{1}{\frac{\pi \, d_j^4}{L_j}\left[\frac{1}{128\,\mu} + \frac{1}{12\,d_j}\sqrt{\left(\frac{8\,R\,T}{\pi\,M}\right)}\left(\frac{1}{P_{mj}}\right)\right]}} \frac{\Delta P \, P_m}{P_2} \tag{10}$$

This expression gives the flow rate as a function of the upstream and downstream pressures applied to the capillary, but also as a function of the mean pressures in each segment, which are unknown. These unknown are solved iteratively. Given the mean pressure distribution at step $(I-1)$, the flow rate in each pore segment is computed according to Eq. (8). We obtain for each segment a flow rate δQ^{I-1}. Because the pressure distribution is not correct (and conservation of mass is not satisfied), this flow rate does not satisfy Eq. (10). A new value of the difference at the inlet and outlet of each segment can be computed according to this equation:

$$\Delta P_j^I = \frac{\delta Q^{I-1} \, P_2}{P_m} \sum_{j=1}^{M} \frac{1}{\frac{\pi \, d_j^4}{L_j}\left[\frac{1}{128\,\mu} + \frac{1}{12\,d_j}\sqrt{\left(\frac{8\,R\,T}{\pi\,M}\right)}\left(\frac{1}{P_{mj}^{I-1}}\right)\right]} \tag{11}$$

and the new distribution of pressure in each segment of the capillary at step *I* can be computed. The calculation starts with a linear distribution of pressure over the capillary and stops when the error defined as:

$$\varepsilon^I = \left(\frac{\delta Q^I - \delta Q^{I-1}}{\delta Q^{I-1}}\right)^2 \quad (12)$$

ε^I is less than a given threshold (10^{-24}). Figure 5 shows the result of such a calculation in the case of a capillary made of three segments of equal length subjected to a difference of pressure of 0.3 MPa. In this case, the iterative scheme converges very rapidly (12 iterations), the logarithm of the error being a nearly linear function decreasing with the number of iterations. In the case of Poiseuille flow, the pressure distribution should be linear. Because of Knudsen effect, the pressure increases in the capillary.

Permeability of the hierarchical capillary bundle

For a given random assembly of capillary fibers, the transport properties are obtained by adding the N_s contributions of each capillary:

$$Q_{tot} = \sum_{i=1}^{N_s} \delta Q_i = \frac{\Delta P\, P_m}{P_2} \sum_{i=1}^{N_s} \frac{1}{\sum_{j=1}^{m(i)} \frac{1}{\frac{\pi d_j^4}{L_j}\left[\frac{1}{128\,\mu} + \frac{1}{12\,d_j}\sqrt{\left(\frac{8RT}{\pi M}\right)}\left(\frac{1}{P_{mj}}\right)\right]}} \quad (13)$$

where $m(i)$ is equal to 1 for capillaries of constant diameter and then $L_j = L_e$. At the macro-scale, the flow rate through the porous medium is described by Darcy's law:

$$Q_D^v = \frac{K_a}{\mu} S \frac{\Delta P\, P_m}{L_e\, P_2} \quad (14)$$

where S is the apparent cross section of the material through which gas flows. Comparison between Eq (13) and Eq (14) provides the expression of the apparent permeability K_a:

$$K_a = \left(\frac{\mu\, L_e}{S}\right) \sum_{i=1}^{N_s} \frac{1}{\sum_{j=1}^{m(i)} \frac{1}{\frac{\pi\, d_j^4}{L_j}\left[\frac{1}{128\,\mu} + \frac{1}{12\, d_j}\sqrt{\left(\frac{8\,R\,T}{\pi\, M}\right)}\left(\frac{1}{P_{mj}}\right)\right]}} \tag{15}$$

This expression may appear rather complex, but the dependence on the average pressure is quite similar to that in Klinkenberg's expression (1941) of the permeability to gas in a porous material. The apparent permeability depends on the inverse of the pressure distribution because Poiseuille's flow is a function of the square of the pressure whereas Knudsen flow is linearly dependent on the pressure. The intrinsic permeability K_{in} is obtained by considering an infinite average pressure:

$$K_{in} = \left(\frac{\mu\, L_e}{S}\right) \sum_{i=1}^{N_s} \frac{1}{\sum_{j=1}^{m(i)} \frac{1}{\frac{\pi\, d_j^4}{L_j}\left[\frac{1}{128\,\mu}\right]}} \tag{16}$$

and it depends on the contribution of Poiseuille's flow only. Recall that the permeability calculated account for an isotropic flux. Hence, it needs to be divided by three in order to compare with the directional permeability obtained next experimentally. We are now are going to describe the experiments carried out in order to evaluate the capabilities of the above model.

EXPERIMENTS

Specimens and testing description

Experiments have been performed on mortars specimens with a water/cement ratio of 0.7 and a maximum aggregate diameter of 3mm. The composition is reported in Table 1. Mortar was cast in aluminum moulds (dimensions: 40x60x400 in mm). Cylindrical holes were moulded by adding metallic bars of diameter 6.5mm in the mould. Finally, a core drill was used to extract a cylindrical hollow specimen (outer diameter=24.5mm; inner diameter=6.5mm; height=40 mm). Note that top and bottom surfaces were rectified using an accurate cutting machine. Finally, the samples were cured in a ventilated oven at 80°C at constant humidity during 48 hours.

368 The testing apparatus consists in a conventional electro-mechanical testing machine (Zwick Proline
369 Z20, maximal force: 20kN) coupled with a nitrogen permeameter in order to measure in-situ the
370 radial permeability under loading (Fig. 6). This set-up is similar to the one implemented by
371 Choinska et al. (2007), but the specimens are much smaller so that they can fit in the mercury
372 intrusion machine.
373 The tests are displacement controlled in order to avoid post-peak unstable regime. Figure 7 presents
374 a typical measurement cycle. A small preload is first applied to seal the upper and lower faces of the
375 specimen so that leakage occurs on the outer circular surface only. The initial permeability is then
376 measured and a given compressive load is applied. Permeability under load and after unloading is
377 measured. Several cycles are performed on different specimens made of the same material in order
378 to describe different states of increasing damage in mortar.
379 After complete unloading, the middle part of each sample (15mm over 40mm) is cut and further
380 used in order to characterize the PSD by mercury intrusion. The same sample cannot be
381 characterized in term of PSD and then loaded again. Nevertheless, the reproducibility of the PSD
382 measurements as well as of the mechanical response of different samples has been checked. Each
383 PSD is obtained as an average of measurements on 3 different specimens.
384
385 *Experimental measurements*
386 Damage D is defined as the relative reduction of the modulus of elasticity upon unloading-
387 reloading:
388
389 $$\sigma = E\,\varepsilon = (1-D)E_0\,\varepsilon\ , \qquad D = 1 - \left(\frac{E}{E_0}\right) \tag{17}$$
390
391 where $(\sigma, \varepsilon, D, E, E_0)$ are respectively the uniaxial stress and strain, the damage parameter and the
392 current and initial elastic moduli.

The apparent permeability is measured by applying a pressure gradient and measuring the gas flow through the sample (Scheidegger, 1974):

$$K_a = \frac{Q_i \mu \ P_i \ln(\frac{R_2}{R_1})}{\pi h (P_i^2 - P_2^2)} \quad (18)$$

Here, nitrogen is used. Q_i is the gas volumetric flow, (h, R_2, R_1) are the sample height, outer and inner diameters respectively and (P_i, P_2) are the gas upstream and downstream pressure respectively. Typically P_2 is the atmospheric pressure and four to five values of the upstream pressure (ranging from 0 to 0.4 MPa) are considered. In order to obtain the intrinsic permeability experimentally, Klinkenberg's formula is implemented:

$$K_a = K_{in} (1 + \frac{\beta}{P_m}) \quad (19)$$

where β is the Klinkenberg's coefficient, K_{in} is the intrinsic permeability and P_m is the mean pressure. β and K_{in} are obtained from the linear regression of the curve giving the apparent permeability as a function of the inverse of the mean pressure.

The PSD measurements are performed by mercury intrusion (Micromeritics–AutoPore IV). The analysis is based on the Washburn equation with the assumption that the pores are cylindrical and connected from the larger pores to the smaller ones. Only the porosity accessible from the outer surface is taken into account. Bottle neck effects are limited by performing two intrusion cycles.

Experimental results

Table 2 presents the mechanical properties of the mortar tested under compression. Figure 8 shows a typical mechanical response of the specimens for different loading-unloading cycles and Figure 9 shows the evolution of damage computed according to Eq. (17). On the horizontal axis, the stress

418 has been normalized by the peak stress. Figure 10 shows the evolution of pore size distribution of
419 samples subjected to different mechanical damage (from 0 to 12%). As damage increases, a slight
420 increase of the PSD is observed between 1,000nm and 3,000nm. Moreover new porosity is created
421 around 10,000nm. This new porosity leads to the increase of the intrinsic permeability by two
422 orders of magnitude. This figure illustrates also the necessity to record low-pressure signals during
423 mercury intrusion. Indeed, as damage develops, micro-cracks form pores with aperture in the range
424 of the measurement of mercury intrusion under low pressure. These pores are major contributors to
425 the increase of permeability and ought to be taken into account in the model.
426 The evolution of the intrinsic permeability and Klinkenberg coefficient upon damage are very
427 similar to those obtained by Choinska et al. (2007) on concrete. They will be compared in the next
428 section against the model results.

429 **COMPARISON BETWEEN EXPERIMENTAL RESULTS AND MODEL**
430 **PREDICTIONS**

431 Figure 11(a) presents the comparison between the measured and computed intrinsic permeability
432 evolution upon damage from 0% to 12%. The computed values are derived from an average of at
433 least 5 hierarchical capillary bundles generated for each average PSD with different random seeds.
434 They are in good agreement with the experimental ones. Note that no tortuosity parameter has been
435 introduced in the model (tortuosity equals 1). Introducing a tortuosity in the model would not,
436 however, change drastically the predictions, e.g. by an order of magnitude.
437 The predicted values are compared to the measurements of the permeability obtained under load.
438 The PSD measurements, which are the only input of the model, are performed after unloading but it
439 seems that the mercury intrusion may have reopened micro-cracks that were closed upon unloading.
440 In these conditions, the porous network characterized by mercury intrusion may be closer to the
441 under-load one than to the unload one.

442 Figure 11(b) shows the evolution of the Klinkerberg's coefficient upon damage. Comparisons
443 between the experimental and theoretical results are plotted. Once again the agreement is rather
444 good whatever the damage state and the predicted values are closer to the under-load ones.
445 The model provides rather good predictions in term of apparent permeability to nitrogen. We have
446 also tested its predictability for other gases. Because their molecular diameter and average free path
447 are different compared to nitrogen, Knudsen's effect will be different too, yielding (along with
448 variations of the viscosity) different evolution of the apparent permeability with pressure. For an
449 undamaged sample, Figure 12 shows the evolution of the apparent permeability to different gases
450 (CO2, CH4, N2, H2) estimated by the model. Table 3 shows the various parameters that enter for
451 each gas in the model. We observe that the responses of CO2, CH4 and N2 are similar whereas the
452 helium response is different. Since the helium mean free path is greater than the nitrogen one,
453 Knudsen effect is higher for helium and then the slope of the apparent permeability vs. mean
454 pressure curve is also higher compared to the other gases.
455 Figure 13 shows the comparison between the apparent permeabilities to nitrogen and helium
456 measured experimentally and computed according to the present model. We observe a good
457 agreement between the experimental and predicted values, both on the intrinsic permeability and on
458 the Klinkenberg's coefficient. It is important to notice that when performing the comparisons, no
459 specific model parameter is set to predict the apparent permeability with the proposed model upon a
460 change of the nature of the gas.

461 **CONCLUSIONS**

462 A semi-analytical model aimed at computing the apparent permeability of a porous material to gas
463 has been presented. The model uses the pore size distribution of the material as an input, including
464 the low-pressure information obtained from mercury intrusion technique.
465 The porous network is generated according to a hierarchical scheme in which pore segments are
466 assembled hierarchically, from large diameters of pores to small ones. Within each capillary pore,
467 fluid flow is described at the micro-scale by a combination of Poiseuille's Flow and Knudsen's

(diffusion) flow. The outcome at the macroscopic scale results into a Klinkerberg-type of apparent permeability, within a Darcy-type equation. The sensitivity of the permeability to the mean pressure is recovered.

The model has been compared with experiments on cylindrical hollow mortar specimens subjected to uniaxial compression and radial permeation. In the case of permeability to nitrogen, the intrinsic permeability increases and the Klinkerberg's coefficient are found to decrease experimentally upon damage. The theoretical model captures these trends very consistently. In addition, the same model is also capable of predicting the permeability of the material to different gas, without any adjustment of the model parameters.

Acknowledgements: Financial supports from the *European Research Council* through the ERC advanced grant Failflow (27769), from the French *Région Aquitaine* through the grant CEPAGE (20121105002) and from the French *Agglomération Côte Basque – Adour* are gratefully acknowledged. F. Khaddour is grateful to the Syrian Ministry of Higher Education for its support (13153/4/W). The authors would like to thank Lionel Ecay for his help.

BIBLIOGRAPHY

Aït-Mokhtar, A., Amiri, O., Dumargue, P., and Sammartino, S. (2002). A new model to calculate water permeability of cement materials from MIP results. *Advances in Cement Research*, Vol. 14(2), 43–49.

Amiri, O., Aït-Mokhtar, A., and Sarhani, M. (2005). Tri-dimensional modelling of cementitious materials permeability from polymodal pore size distribution obtained by mercury intrusion porosimetry tests. *Advances in Cement Research*, Vol.17(1), 39–45.

Arson, C. and Pereira, J.M. (2013). Influence of Damage on pore size distribution and permeability of rock, *Int. J. Numer. Anal. meth. Geomechanics*, Vol. 37, 810-831.

Berndt, E. and Sevostianov, I. (2012). Multiscale modeling of fluid permeability of a non-homogeneous porous media, *Int. J. Engrg. Sciences*, Vol. 56, 99-110.

494 Blunt, M.J. (2001). Flow in porous media - Pore network models and multiphase flow, *Current*
495 *Opinions in Colloïd and Interface Science,* Vol. 6, 197-207.
496 Blunt, M.J., Jackson, M.D., Piri, M., and Valvatne, P.H. (2002). Detailed physics, predictive
497 capabilities and macroscopic consequences for pore-network models of multiphase flow, *Advances*
498 *in Water Res.*, Vol. 25, 1069-1089.
499 Brown, P.W., Shi, D., and Skalny, J.P. (1991). Porosity/permeability relationships, *Material*
500 *Science of Concrete II*, J. Skalny and S. Mindess Eds., American Ceramic Society, Westerville OH.,
501 83-109.
502 Chen, W., La Borderie, C., Maurel, O., Pijaudier-Cabot, G., Rey-Betbeder, F. (2014). Simulation of
503 Damage - Permeability Coupling for Mortar under Dynamic Loads, *Int. Num. Anal. Meth.*
504 *Geomechanics*, Vol. 38, 457-474.
505 Childs, E.C. and Collis-George, N. (1950). The permeabilityof porous materials, *Proc. Royal Soc.,*
506 London, 201A, 392.
507 Choinska, M., Khelidj, A., Chatzigeorgiou, G., and Pijaudier-Cabot, G. (2007). Effects and
508 Interactions of Temperature and Stress-Level Related Damage on Permeability of Concrete. *Cement*
509 *Concr. Res.,* Vol. 37, 79–88.
510 Chunsheng, Z., Kefei, L. Xiaoyun, P. (2011). Effect of crack density and connectivity on the
511 permeability of microcracked solids, *Mech. Mats.*, Vol. 43, 969-978.
512 Darcy, H. (1856). Les fontaines publiques de la ville de Dijon,. *Dalmont, Paris*.
513 Diamond, S. (2000). Mercury porosimetry - an inappropriate method for the measurement of pore
514 size distributions in cement-based materials, *Cement and Concr. Res.*, Vol. 30, 1517-1525.
515 Dormieux, L., Kondo, D., and Ulm, F.J. (2006. *Microporomechanics*, Wiley Pubs. London U.K.,
516 Grassl, P. (2009). A lattice approach to model flow in cracked concrete, *Cement and Concr.*
517 *Composites,* Vol. 31, 454-460.
518 Gueguen, Y., and Dienes, J. (1989). Transport properties of rocks from statistics and percolation,
519 *Math. Geology,* Vol. 21, 1.

Hoseini, M., Bindiganaville, V., and Banthia, N. (2009). The effect of mechanical stress on permeability of concrete: A review, *Cement and Concr. Composites,* Vol. 31, 213-220.

Jason, L., Pijaudier-Cabot, G., Ghavamian, S., and Huerta, A. (2007). Hydraulic behaviour of a representative structural volume for containment buildings, *Nuclear Engrg. Design*, Vol. 237, 1259-1274.

Kast, W., and Hohenthanner, C.-R. (2000). Mass transfer within the gas-phase of porous media. *International Journal of Heat and Mass Transfer*, Vol. 43(5), 807–823.

Katz, A.J. and Thompson, A.H. (1986). Quantitative prediction of permeability in porous rock. *Physical review*, Vol. 34(11), 8179–8181.

Khaddour, F., Grégoire, D., and Pijaudier-cabot, G. (2013). Upscaling Permeation Properties in Porous Materials from Pore Size Distributions. *Geomechanical Issues in CO2 Storage Facilities*, G. Pijaudier-Cabot and J.M. Pereira Eds., ISTE Wiley Pubs., London U.K., 44–56.

Khaddour, F., Gregoire, D., Pijaudier-Cabot, G. (2014). Computing permeation properties of mortar from pore size distributions, Computational Modelling of Concrete Structures - Proc. Euro-C conf. held in St. Anton, Austria, N. Bicanic, H. Mang, G. Meschke, and R. de Borst eds., CRC press, Vol. 1, 405-414.

Khaddour, F., Grégoire, D., and Pijaudier-Cabot, G. (2015). Capillary bundle model for the computation of the apparent permeability from pore size distributions. *European journal of environmental and civil engeneering*, Vol. 19, 168-183.

Klinkenberg, L. J. (1941). The permeability of porous media to liquids and to gases. *API Drilling and Production Practice*, 200–213.

Kozeny, J. (1927). Ueber kapillare Leitung des Wassers im Boden''. *Wien, Akad. Wiss*, Vol. 136(2a), 271.

Li, K., Stroeven, M., Stroeven, P., and Sluys, L.J. (2016). Investigation of liquid water and gas permeability of partially saturated cement paste by DEM approach, *Cement Concr. Res.*, Vol. 83, 104-113.

546 Miehe, C., Mauthe, S. (2016). Phase field modeling of fracture in multi-physics problems. Part III.
547 Crack driving forces in hydro-poro-elasticity and hydraulic fracturing of fluid-saturated porous
548 media, *Computer Methods in Applied Mechanics and Engineering*, Vol. 304, 619-655.
549 Pijaudier-Cabot, G., Dufour, F., Choinska, M. (2009). Permeability Due to the Increase of Damage
550 in Concrete: From Diffuse to Localised Damage Distributions, *J. Engrg. Mech. ASCE*, 135, 1022 –
551 1028.
552 Poiseuille, J.L.M. (1840). Physique-Recherches expérimentales sur le mouvement des liquides dans
553 les tubes de très petits diamètres, Academie des sciences. *Academie des sciences , comptes rendus-*
554 *in French*, *11*, 961–967 and 1041–1048.
555 Rahmanian, M. R., Aguilera, R., and Kantzas, A. (2013). A New Unified Diffusion — Viscous-
556 Flow Model Based on Pore-Level Studies of Tight Gas Formations. *Society of Petroleum*
557 *Engineers*, Vol. 18(1), 38–49.
558 Scheidegger, A. E. (1974). The physics of flow through porous media. *University of Toronto Press*.
559 Steckelmacher, W. (1986). Knudsen flow 75 years on: the current state of the art for flow of
560 rarefied gases in tubes and systems. *Rep. Prog. Phys*, Vol. 49, 1083–1107.
561 Sun, W.C., Andrade, J.E, Rudnicki, J.W. (2011). A multiscale method for characterization of
562 porous microstructures and their impact on macroscopic effective permeability, *International*
563 *Journal for Numerical Methods in Engineering*, Vol. 88, 1260-1279.
564 Sun, W.C., Kuhn, M.R., Rudnicki, J.W. (2013). A multiscale DEM-LBM analysis on permeability
565 evolutions inside a dilatant shear band, *Acta Geotechnica*, Vol. 8, 465-480.
566 Timothy, J.J., and Meschke, G. (2016). A cascade lattice micromechanics model for the effective
567 permeability of materials with microcracks, *Journal of nanomechanics and Micromechanics, ASCE*,
568 Vol. 6, NM.2153-5477.0000113.
569 White, J. A., Borja, R. I., & Fredrich, J. T. (2006). Calculating the effective permeability of
570 sandstone with multiscale lattice Boltzmann/finite element simulations. *Acta Geotechnica*, Vol. 1,
571 195-209.

572 Wong, H.S., Zimmerman, R.W., and Buenfeld, N.R. (2012). Estimating the permeability of cement
573 pastes and mortar using image analysis and effective medium theory, *Cement Concr. Res.,* Vol. 42,
574 476-483.
575 Ziarani, A.S. and Aguilera, R. (2012). Knudsen's permeability correction for tight porous media,
576 *Transp. Porous Med.,* Vol. 91, 239-260.
577

Table1. Mortar composition.

Ingredient	Water	Cement	Sand	W/C ratio
Quantity (kg/m^3)	243	412	1651	0.7

Table2. Mechanical properties of mortar.

Modulus of Young (GPa)	Resistance to compression (Mpa)	Strain at peak (%)
20	29	0.21

Table 3. Physical parameters for each gas obtained from NIST database (http://webbook.nist.gov/chemistry/)

Type of gas	N_2	He	CO_2	CH_4
Molar mass (kg/mol)	0.0280134	0.0040026	0.0440095	0.0160425
Viscosity (Pa.s)	0.0000174	0.0000199	0.00001469	0.000011026
Molecular diameter (A°)	3,64	2,6	3,3	3,8

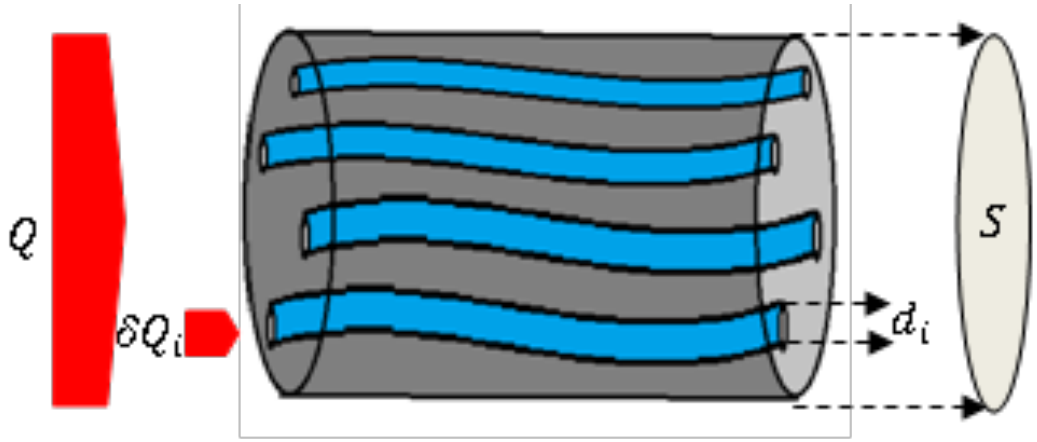

Figure 1.Model of parallel assembly of pores

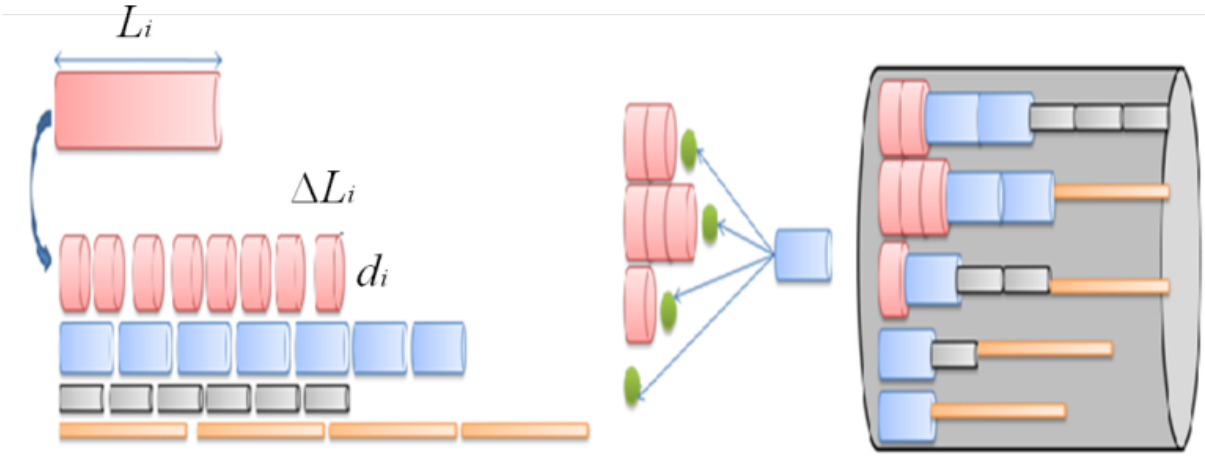

(a). Discretization of pores (b). Random assembly

Figure 2. Random network assembly of pores

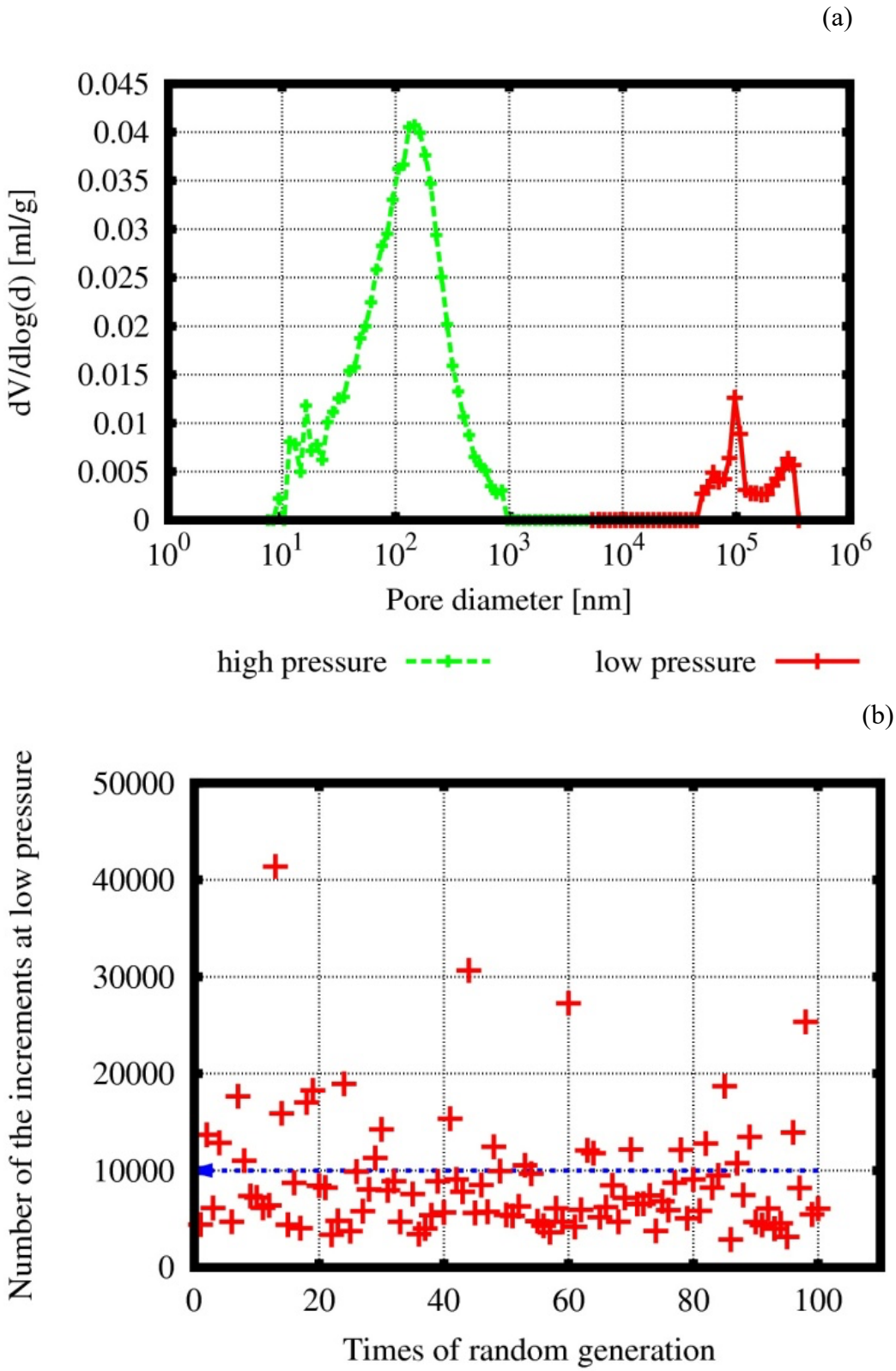

Figure 3. Method of eliminating of the noise at low pressure for an undamaged sample a) pore size distribution corresponding to the low and high pressures b) statistical study of the low frequency for 100 random times

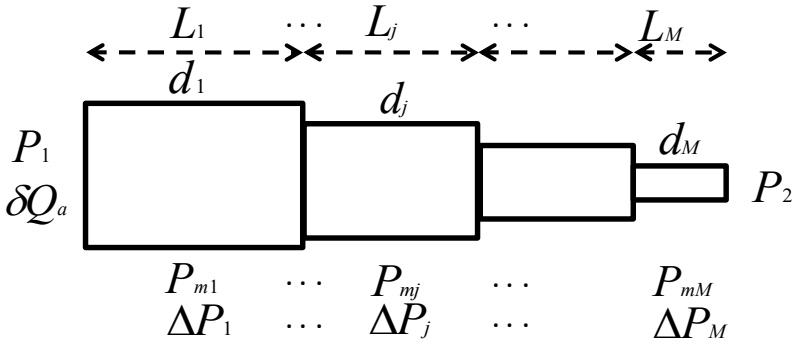

Figure 4. : Capillary made of segments with decreasing diameter

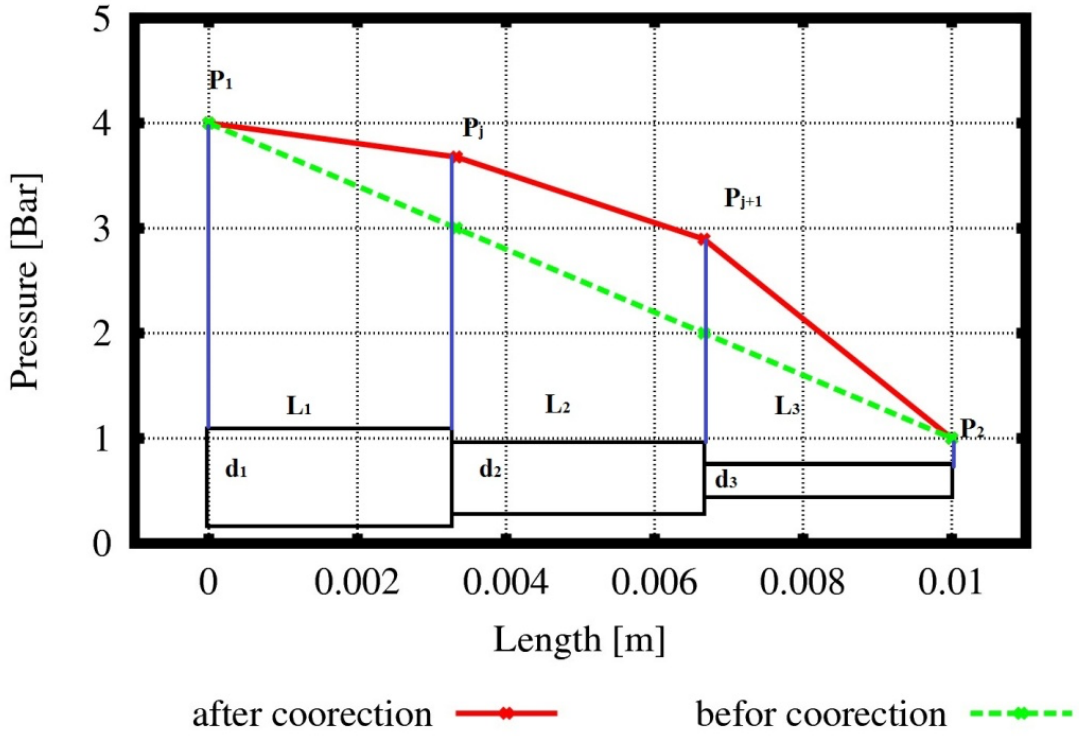

Figure 5. Distribution of pressure in a capillary made of three segments with decreasing diameter at the initial iterative scheme and after convergence.

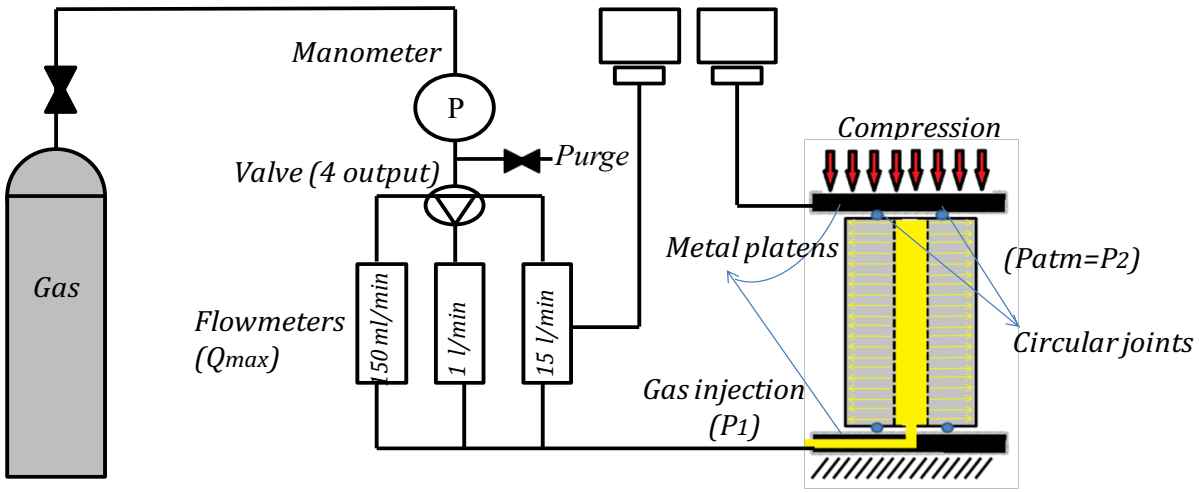

Figure 6. Schematic description of the mechanical and permeability tests

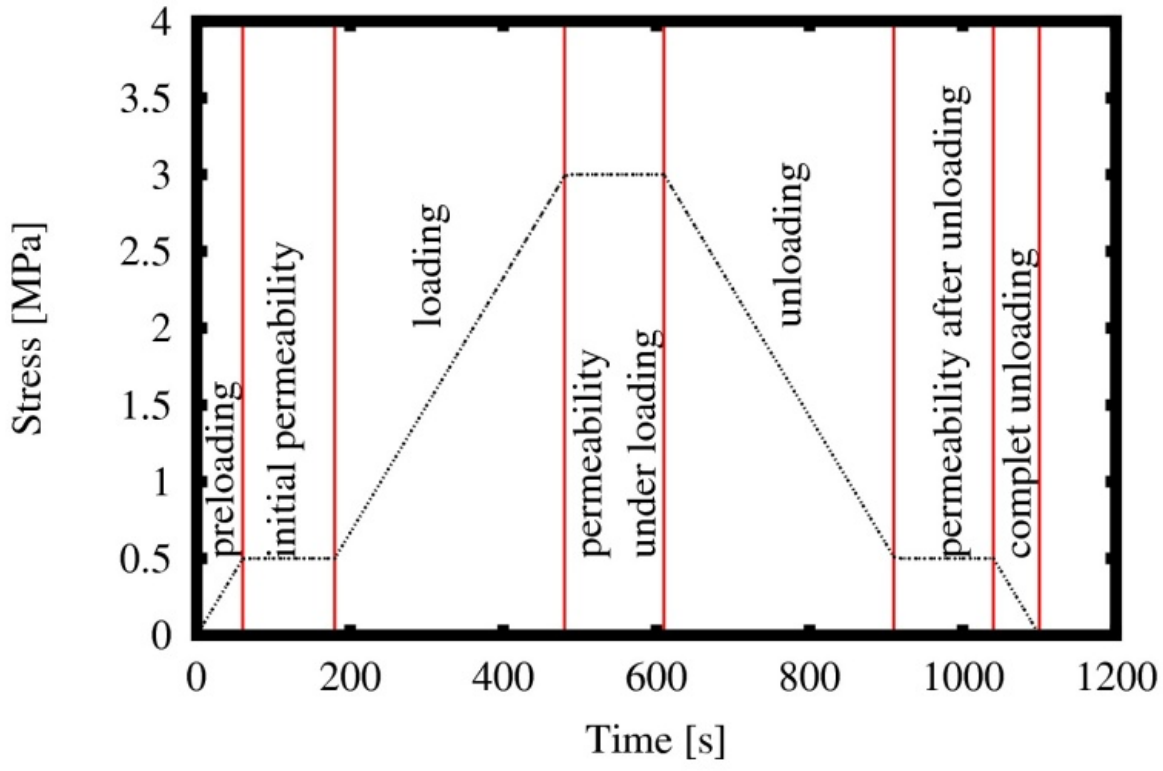

Figure 7. Load vs time curve

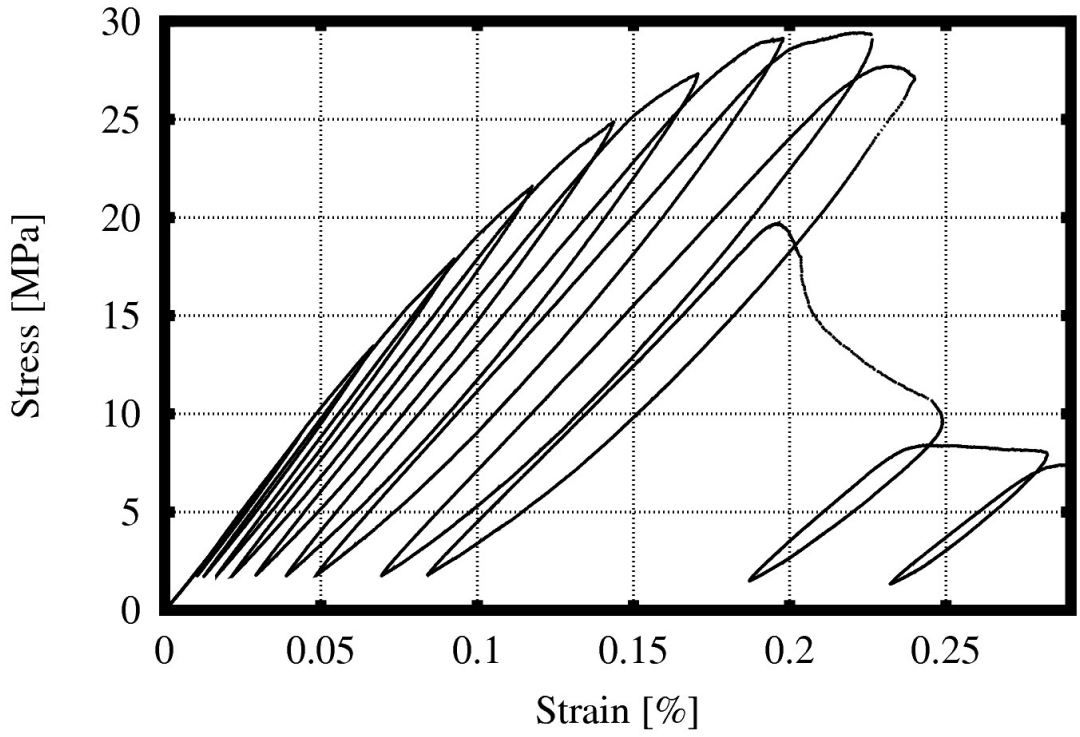

Figure 8. Typical stress-strain curve of a mortar sample

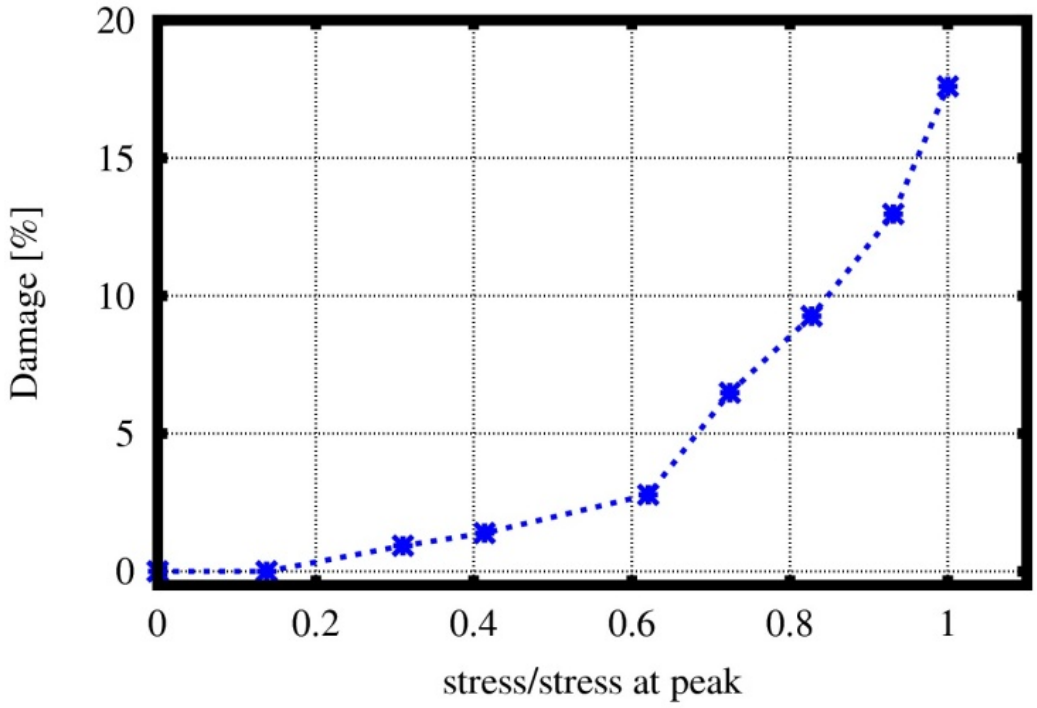

Figure 9. Damage-stress/stress at peak curve of the specimens

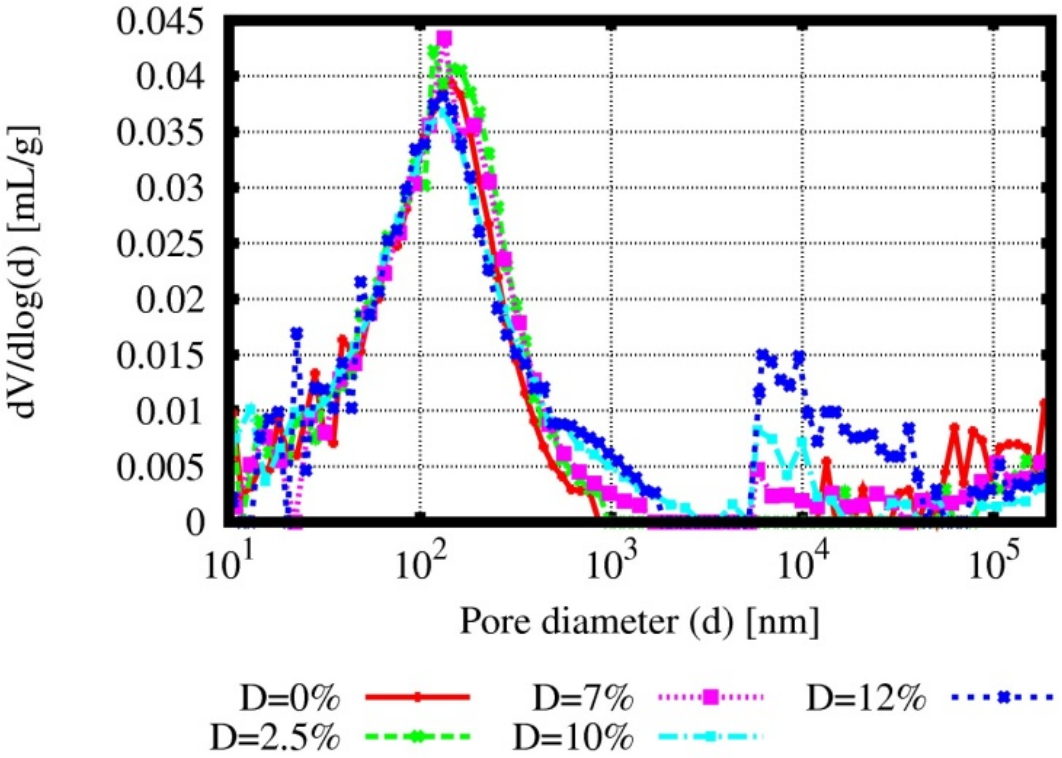

Figure 10. Evolution of pore size distribution upon damage

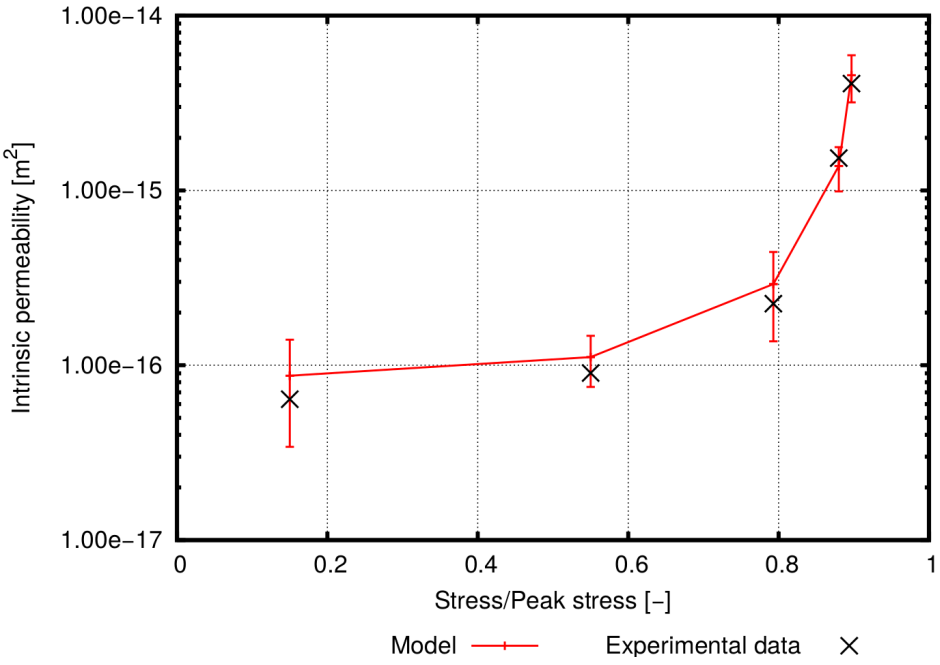

(a) Intrinsic permeability

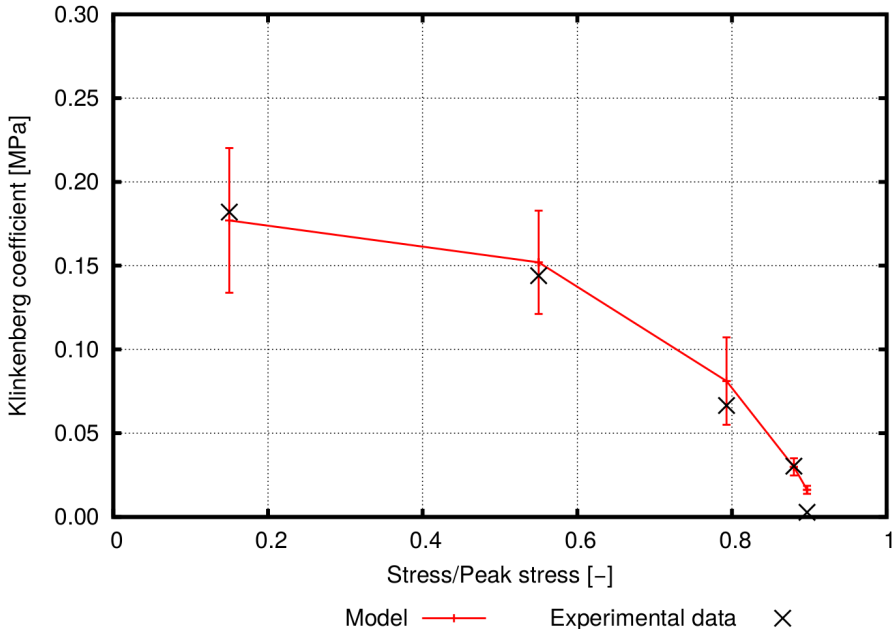

(b) Klinkenberg coefficient

Figure 11. Comparison between the intrinsic permeability measured and predicted (a); comparison between the Klinkenberg's coefficient measured and predicts (b).

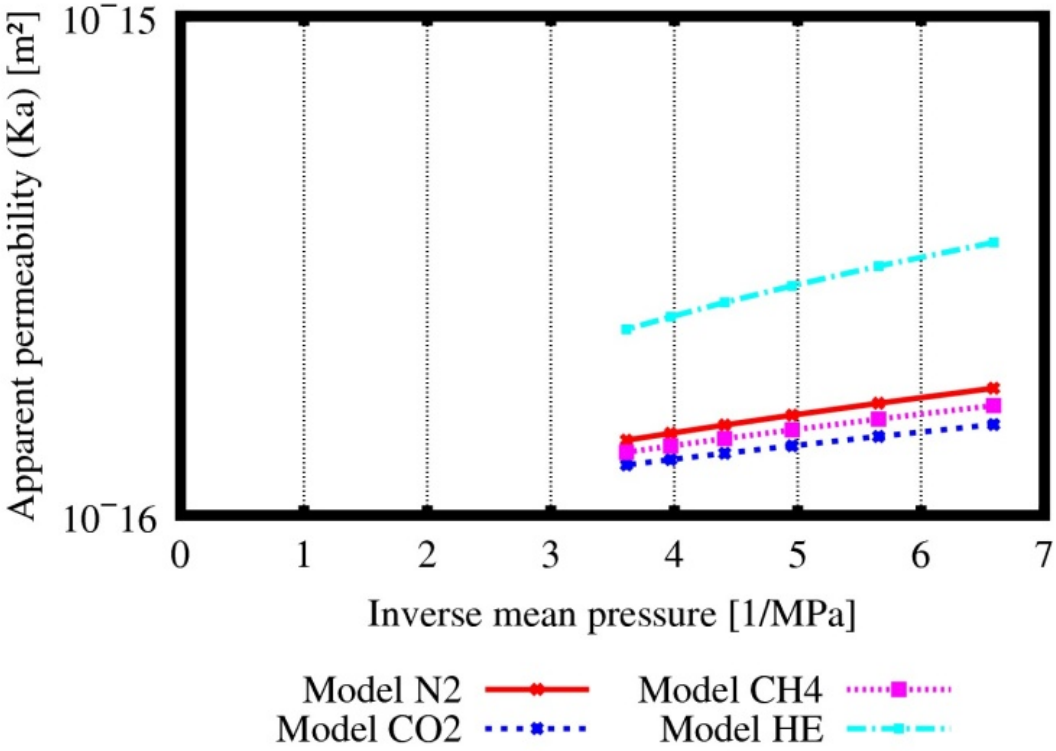

Figure 12. Evolution of the apparent permeability for several gases (CO_2, CH_4, N_2, He)

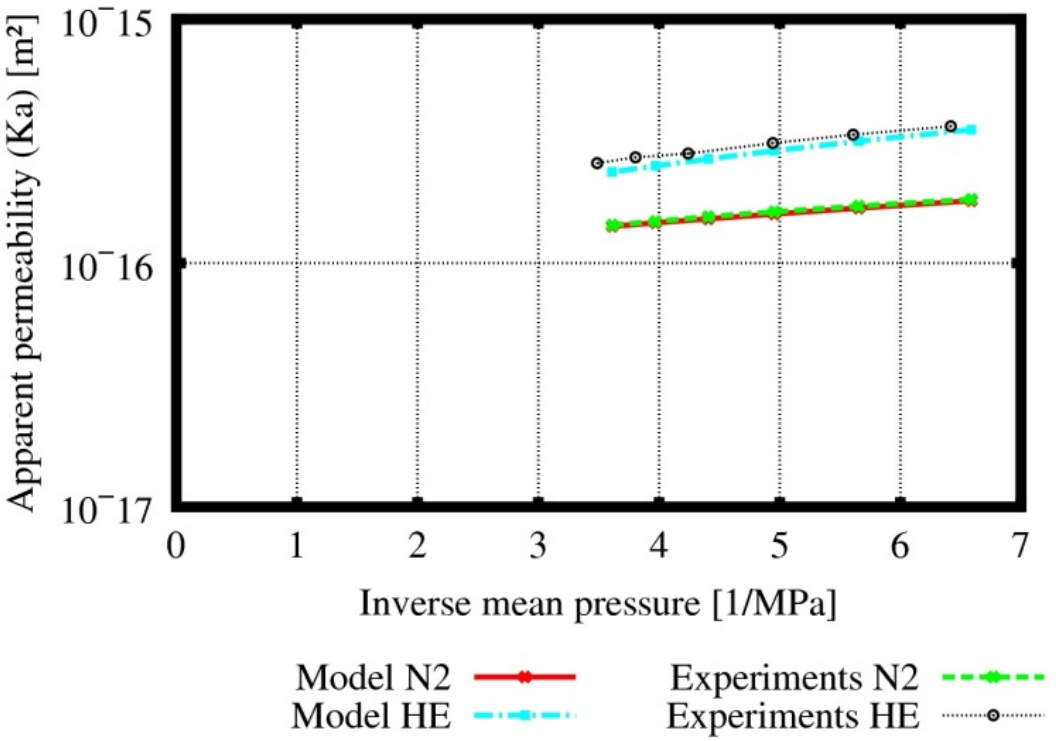

Figure 13. Comparison between the model and the experimental results of apparent permeabilities for N_2 and He.